# Grazing-incidence resonant elastic x-ray scattering of skyrmion lattices in bulk MnSi

Jingyi Chen,[1] Andreas Bauer,[2,3] Christian Pfleiderer,[2,3,4,5] Gerrit van der Laan,[6]
Thorsten Hesjedal,[6,7,*] and Shilei Zhang[1,8,9,†]

[1]*School of Physical Science and Technology, ShanghaiTech University, Shanghai 201210, China*
[2]*Physics Department, TUM School of Natural Sciences, Technical University of Munich, D-85748 Garching, Germany*
[3]*TUM Center for QuantumEngineering (ZQE), Technical University of Munich, D-85748 Garching, Germany*
[4]*Munich Center for Quantum Science and Technology (MCQST), D-80799 Munich, Germany*
[5]*Heinz Maier-Leibnitz Zentrum (MLZ), Technical University of Munich, Lichtenbergstraße 1, D-85747 Garching, Germany*
[6]*Diamond Light Source, Harwell Science and Innovation Campus, Didcot OX11 0DE, United Kingdom*
[7]*Department of Physics, Clarendon Laboratory, University of Oxford, Oxford OX1 3PU, United Kingdom*
[8]*ShanghaiTech Laboratory for Topological Physics, ShanghaiTech University, Shanghai 201210, China*
[9]*Center for Transformative Science, ShanghaiTech University, Shanghai 201210, China*

(Received 28 February 2026; revised 14 May 2026; accepted 16 July 2026; published 14 August 2026)

Magnetic skyrmions are spin textures with nontrivial topology that form two-dimensional hexagonal lattices (SkX) in chiral magnets. Element-specific reciprocal-space characterization of skyrmion lattices with soft x-rays commonly relies on transmission geometries, which require thinning of bulk crystals and can modify their magnetic properties. Here, we show that resonant elastic x-ray scattering in a grazing-incidence geometry (GIREXS) provides a nondestructive and geometrically flexible probe of skyrmion lattices in bulk materials. Using MnSi as a model system, GIREXS resolves the helical, conical, and skyrmion-lattice states through their characteristic magnetic satellite peaks and yields the skyrmion wave vector. By operating just above the critical angle ($\alpha_c \approx 1.6°$ in MnSi at the Mn $L_3$ edge), the method achieves a probing depth of approximately 3 nm, tunable up to approximately 20 nm via the incidence angle, while maintaining full reciprocal-space access to the in-plane magnetic correlations. The grazing-incidence approach circumvents the structural Bragg-peak constraints that limit conventional reflection resonant elastic x-ray scattering (REXS) at fixed soft-x-ray energies. Our measurements establish GIREXS as a practical method for studying magnetic superstructures in bulk crystals, providing direct reciprocal-space access to magnetic satellite reflections and a basis for future depth-controlled, element-selective investigations of complex spin textures.

DOI: 10.1103/1788-7m8w

## I. INTRODUCTION

Magnetic skyrmions are topologically stable, vortex-like spin textures that hold potential for next-generation spintronic devices due to their nanoscale size, relative stability, and the low energy required to manipulate them. The skyrmion lattice was first observed in the noncentrosymmetric B20 compound MnSi by small-angle neutron scattering [1]. Subsequently, a distinct topological contribution to the Hall effect was identified in the MnSi A-phase [2], and the associated emergent electrodynamics was investigated in detail [3]. These properties establish MnSi as a model system for exploring the fundamental physics of skyrmions and assessing their potential for applications in data storage and computing. Here, we implement grazing-incidence resonant elastic x-ray scattering (GIREXS) as a nondestructive, element-specific reciprocal-space probe of skyrmion-lattice order in bulk crystals, demonstrated on MnSi as a model chiral magnet.

MnSi is a cubic B20 chiral magnet with a Curie temperature of $T_C \approx 29$ K [1] and a well-established magnetic phase diagram. The absence of inversion symmetry gives rise to the Dzyaloshinskii-Moriya interaction that competes with ferromagnetic exchange and stabilizes a long-wavelength helical ground state with a period of

*Contact author: thorsten.hesjedal@physics.ox.ac.uk
†Contact author: shilei.zhang@shanghaitech.edu.cn

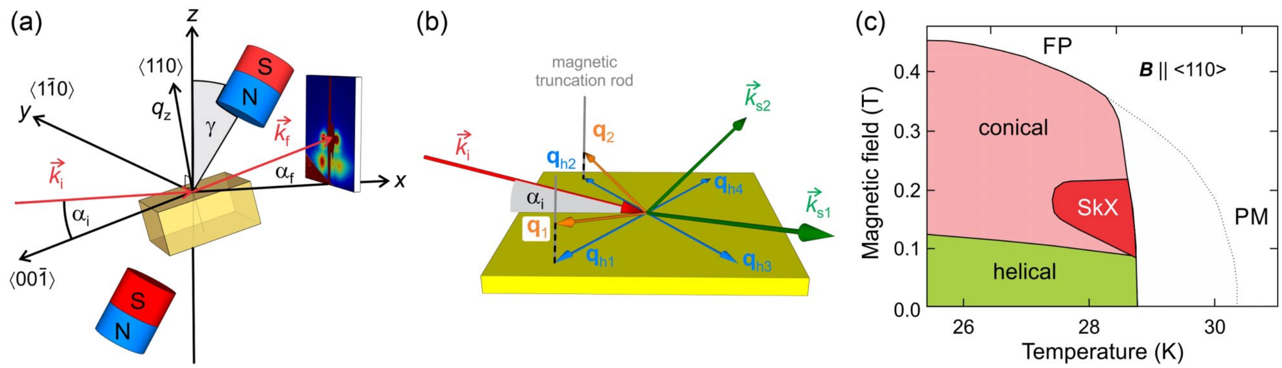


FIG. 1. Grazing-incidence REXS geometry and experimental setup for the measurement of the magnetic phases in bulk MnSi. (a) Experimental scattering geometry showing the orientation of the [110]-cut MnSi single crystal and applied magnetic field. The incident soft x-rays are tuned to the Mn $L_3$ edge (641.3 eV) and linearly $\sigma$-polarized. The incident angle $\alpha_i$ is chosen typically between 0° and 10° (above the critical angle of approximately 1.6°). The beam footprint therefore covers a sample area of several $mm^2$. The scattered x-rays are collected with a CCD camera, allowing for the detection of off-specular magnetic satellites. A rotatable permanent magnet pair applies magnetic fields up to 180 mT at an angle $\gamma$ relative to the surface normal (here, $\gamma = 0°$). (b) Schematic view of the reciprocal-space geometry in the helical phase. Due to the finite exit angle $\alpha_f$, the scattered wavevectors $\vec{k}_s$ acquire out-of-plane components, resulting in momentum transfers with finite $\vec{q}_z$. This enables detection of lateral magnetic modulations ($\mathbf{q}_{h1}-\mathbf{q}_{h4}$ from the two helical in-plane domains) via off-specular scattering, despite the propagation vectors being strictly in-plane. The blue arrows represent the accessible momentum transfer vectors due to the helical modulations. The lifting of $\vec{q}$ out of the sample plane due to the finite exit angle generates MTRs (two indicated in light gray) associated with the termination of the in-plane magnetic modulation at the surface, enabling detection of lateral modulations in off-specular geometry. Note that $\vec{k}_i$, $\vec{k}_{s1}$, and $\vec{q}_1$ are coplanar, forming the scattering plane for this configuration. (c) Magnetic phase diagram of bulk MnSi for the magnetic field applied along ⟨110⟩. At low fields, the system exhibits a helical ground state that transitions to a conical phase above the lower critical field, and to a field-polarized (FP) phase at high fields. Near $T_C \approx 29$ K, a skyrmion lattice (SkX) phase appears in a narrow field window. At higher temperatures, the system becomes paramagnetic (PM).

approximately 180 Å, much larger than and incommensurate with the atomic lattice ($a = 4.558$ Å). With increasing magnetic field, the helical state evolves into a conical phase and ultimately into a field-polarized state. Close to $T_C$, thermal fluctuations stabilize a skyrmion lattice within a small pocket of the $B$–$T$ phase diagram [4], as shown in Fig. 1(c). Similar phase diagrams have been reported for other B20 helimagnets, including $Fe_{1-x}Co_xSi$ [5,6], $Mn_{1-x}Fe_xSi$ [7], FeGe [8–11], and $Cu_2OSeO_3$ [12]. Thickness and strain in thinned B20 lamellae can also modify the phase diagram [13].

Several complementary experimental techniques have been employed to investigate skyrmion phases in MnSi and related B20 compounds in both bulk and reduced-dimensional geometries. Small-angle neutron scattering (SANS) directly resolves the periodic magnetic modulation in reciprocal space and established the hexagonal skyrmion lattice in bulk MnSi [1,14–16]. Lorentz transmission electron microscopy (LTEM) provides real-space imaging of skyrmion textures and has been widely applied to electron-transparent lamellae of MnSi and other B20 materials [6,12,17–19]. Magnetic force microscopy (MFM) probes surface stray-field contrasts and has been used to visualize skyrmions in bulk crystals [20]. While these techniques have yielded detailed insight into skyrmion textures, each has practical constraints that can limit either sample geometry, probing depth, or reciprocal-space access. SANS requires macroscopic sample volumes and is therefore not well suited to thin films. LTEM relies on thinned specimens, where geometric confinement and reduced dimensionality can modify the magnetic phase diagram [13]. MFM provides surface-sensitive contrast but does not directly access bulk reciprocal-space correlations. In B20 helimagnets, the skyrmion pocket in the $T$–$H$ phase diagram expands systematically with decreasing sample thickness, resulting in an enlarged stability region compared with bulk crystals [13]. Consequently, magnetic phase diagrams derived from lamellae do not necessarily represent intrinsic bulk behavior. This distinction is particularly relevant for MnSi, where reduced dimensionality and strain are known to modify the magnetic phase diagram.

Resonant elastic x-ray scattering (REXS) is a synchrotron-based technique that combines reciprocal-space sensitivity with element selectivity [21,22]. By tuning the photon energy to an absorption edge, REXS enables magnetic contrast with vectorial spin sensitivity and time resolution [23–32]. In grazing-incidence geometries, resonant magnetic x-ray scattering has previously been employed to probe magnetic truncation rods (MTRs) and near-surface magnetic order [33–35], where the termination of bulk magnetic order at the surface gives rise to rods of magnetic scattering analogous to structural crystal truncation rods. Theoretical descriptions have shown that structural and magnetic interfaces can in general differ and that their correlation determines the specular and diffuse magnetic response [36,37]. In the present analysis, we assume that structural and magnetic interfaces coincide and neglect additional interface roughness effects, focusing on the dominant magnetic modulation within the near-surface probing depth. Note that for incommensurate magnetic structures, such as skyrmion lattices, the magnetic satellites decorate structural Bragg reflections. Since the photon energy is fixed by the chosen absorption edge (typically the $3d$ transition-metal $L_3$ edge), the corresponding wavelength is not freely tunable. As a result, many B20 compounds cannot be accessed in conventional reflection geometry. For MnSi ($a = 4.558$ Å [38]) at the Mn $L_3$ edge (641.3 eV, $\lambda = 1.933$ nm), $\lambda > 2a$, and the (001) Bragg condition cannot be satisfied in reflection geometry. An analogous limitation applies to FeGe ($a = 4.689$ Å [39]) at the Fe $L_3$ edge. In contrast, for $Cu_2OSeO_3$ ($a = 8.925$ Å [40]) at 931.1 eV ($\lambda = 1.332$ nm), the (001) structural reflection is accessible at $2\theta = 96.4°$ (see Table I). More generally, this fixed wavelength prevents the use of soft-x-ray REXS for all B20 helimagnets with small lattice parameters, motivating an approach that does not depend on satisfying a structural Bragg condition.

Reflection-geometry REXS is well established for probing magnetic satellite reflections in bulk single crystals when an appropriate structural Bragg reflection is accessible at the resonant wavelength, as demonstrated for the skyrmion lattice in $Cu_2OSeO_3$ [41] and cycloidal antiferromagnetic order in bulk $BiFeO_3$ [42]. The limitation addressed here is therefore not the general feasibility of reflection-mode magnetic scattering from bulk crystals, but the reciprocal-space constraint imposed by the fixed soft-x-ray wavelength. For MnSi, FeGe, and most other B20 compounds with small lattice parameters, the relevant structural Bragg reflections are inaccessible (Table I), precluding conventional reflection-geometry access to the associated magnetic satellites.

This geometric constraint can be relaxed in transmission geometry, where resonant small-angle x-ray scattering detects magnetic satellites around the directly transmitted (000) beam. Such approaches have been successfully applied to several skyrmion-hosting systems, including FeGe [43,44], $Cu_2OSeO_3$ [44,45], and $Co_8Zn_8Mn_4$ [46,47]. However, at soft-x-ray energies the absorption length is limited, requiring samples to be prepared as thin lamellae, thereby reintroducing the dimensionality constraints discussed above for LTEM [48]. Related x-ray imaging techniques, such as scanning transmission x-ray microscopy and x-ray holography [49], provide real-space access to skyrmion textures under cryogenic conditions and applied magnetic fields, but likewise rely on x-ray-transparent specimens. Specular soft-x-ray reflection geometries have recently demonstrated sensitivity to chiral surface spin textures in FeGe and $Cu_2OSeO_3$ [50,51], highlighting the capability of resonant reflection to probe near-surface magnetism without thinning; however, reciprocal-space resolution of a full skyrmion lattice in bulk B20 compounds with small lattice parameters remains geometrically constrained.

TABLE I. Comparison of skyrmion lattice (SkX) parameters, $L_3$ absorption edge energies, and relevant structural properties for selected chiral magnets [41].

| Material | $\lambda_{SkX}$ (Å) | $L_3$ (eV) | $\lambda_{x\text{-ray}}$ (Å) | $a$ (Å) | $2\theta$ (struct. peak) |
|---|---|---|---|---|---|
| MnSi | 180 | 641.3 | 19.33 | 4.558 | … |
| FeGe | 700 | 708.1 | 17.51 | 4.689 | … |
| $Cu_2OSeO_3$ | 620 | 931.1 | 13.32 | 8.925 | 96.4° |

These constraints motivate the development of approaches that enable magnetic scattering without relying on structural Bragg reflections. Here, we implement a grazing-incidence REXS geometry that circumvents the structural Bragg condition inherent to conventional reflection measurements by exploiting MTRs generated by the termination of the in-plane magnetic modulation at the crystal surface. Operating close to the critical angle enhances surface sensitivity while enabling access to in-plane magnetic satellites associated with the helical, conical, and skyrmion-lattice states in bulk MnSi. By tuning the photon energy to the Mn $L_3$ edge, the method directly resolves magnetic diffraction signals from the skyrmion lattice in the topmost approximately 20 nm of an unthinned bulk single crystal. Because no thinning is applied, the magnetic phase diagram in the probed volume is that of the bulk material, while the grazing-incidence geometry simultaneously confers sensitivity to any near-surface modifications of the spin texture. This establishes grazing-incidence resonant x-ray scattering as a practical approach for studying complex spin textures in bulk crystals and for future depth-controlled investigations of skyrmion phases in thin films and heterostructures, with an accessible depth range of approximately 3–20 nm via incidence-angle tuning at the resonance, extendable to several hundred nm by detuning a few eV below the edge, and a depth resolution of approximately 2–3 nm set by the $\alpha_i$ step size. This range is well matched to typical layer thicknesses in magnetic heterostructures.

## II. EXPERIMENTAL DETAILS

The [110]-oriented MnSi single crystal investigated in this study measured approximately $15 \times 11 \times 2.5$ mm$^3$, and the surface was polished to a mirror finish. It was previously used for SANS experiments that confirmed the presence of a skyrmion lattice state [52]. High-resolution x-ray diffraction using both Cu and Mo K$\alpha$ radiation yielded a full-width at half maximum of 0.0177° (for Cu) for the rocking curve of the (110) reflection, indicating excellent crystalline quality.

In REXS [53], when the photon energy is tuned to an absorption edge, the scattering cross section is resonantly enhanced, providing a means of probing subtle changes in spin texture or lattice modulations. This technique has proven invaluable in studies of helimagnets and skyrmion-hosting materials, such as $Cu_2OSeO_3$ [41], where the large lattice constant ($a = 8.93$ Å) permits access to structural Bragg peaks under soft x-ray excitation. Recent work has shown that circular dichroism in specular reflection geometry (at approximately 36°) can be used to detect surface chiral features in $Cu_2OSeO_3$ using soft x-rays [51]. While promising, the skyrmion phase itself was not resolved in reciprocal space in that specular reflection geometry, reflecting the geometric constraints imposed by fixed soft-x-ray wavelengths.

Grazing-incidence small-angle x-ray scattering (GISAXS) is a powerful technique for investigating nanoscale structural features at surfaces and interfaces [54,55]. By directing an x-ray beam at a shallow incident angle, typically just above the critical angle for total external reflection, the penetration depth of the x-rays is limited to the near-surface region, enhancing sensitivity to thin film morphology, lateral ordering, and buried interfaces. GISAXS captures both specular and diffuse scattering, providing access to the full momentum transfer vector $\mathbf{q} = (q_x, q_y, q_z)$, which enables analysis of in-plane correlation lengths, vertical structure, and surface roughness. In the presence of periodic order truncated at a surface, the scattering intensity is distributed along crystal truncation rods; for magnetic order, this gives rise to MTRs that encode the termination of the magnetic modulation at the interface. This versatility makes GISAXS indispensable for studying self-assembled nanostructures, magnetic multilayers, and correlated electronic phases in low-dimensional systems [54,55].

A magnetic extension of GISAXS, GIREXS or resonant magnetic SAXS [56], combines this surface-sensitive geometry with element- and spin-specific contrast by tuning the x-ray energy to a resonant absorption edge. In this approach, linearly or circularly polarized soft x-rays are tuned to resonant edges such as the Fe $L_3$ edge, enhancing sensitivity to magnetic ordering and allowing the detection of nanoscale spin textures [50,56]. To verify the magnetic origin of the observed contrast, the measurement is typically repeated under off-resonance conditions (e.g., 5 eV below the $L_3$ edge), which suppresses the magnetic satellite intensity. The scattering geometry emphasizes low-angle features, akin to GISAXS in the structural context, but with polarization-resolved magnetic contrast. In this geometry, the incident and scattered beams make only a few degrees with respect to the sample surface, and the momentum transfer components $q_y$ and $q_z$ can be extracted from the two-dimensional scattering patterns.

For MnSi, the use of soft x-rays near the Mn $L_3$ edge (approximately 641 eV) results in a wavelength of approximately 19.4 Å, such that the corresponding Ewald sphere is strongly curved on the scale of the magnetic modulation. This geometric factor enhances the visibility of truncation-rod features and Yoneda wings (enhanced surface scattering near the critical angle); the latter were observed in our setup at $\alpha_f \approx 1.53°$ and provide an experimental handle on the critical angle and surface properties. The configuration used at the RASOR endstation at beamline I10 at the Diamond Light Source (Oxfordshire, UK), illustrated in Fig. 1(a), closely matches standard grazing-incidence diffraction geometry with the detector placed near $2\theta \approx 0°$, ensuring high sensitivity to diffuse surface scattering and magnetic Bragg peaks arising from lateral ordering in the near-surface region. In RASOR, a pair of permanent magnets is mounted on sliders on a rotation stage, providing variable magnetic fields of up to 180 mT at arbitrary angle $\gamma$ with respect to the surface normal (in this study, we used $\gamma = 0°$, i.e., field normal to the surface). The setup permits reconstruction of the momentum transfer vector $\mathbf{q} = (q_x, q_y, q_z)$ from specular and off-specular scattering components. In this geometry, the in-plane components $(q_x, q_y)$ probe lateral modulations, such as helical or skyrmion lattices, while the out-of-plane component $q_z$ becomes accessible through variation of $\alpha_f$ at fixed $\alpha_i$. Even for magnetic modulation vectors that lie strictly in-plane, the grazing-incidence geometry with finite exit angle $\alpha_f$ introduces a nonzero vertical component to the scattered wavevector $\vec{k}_s$, resulting in a momentum transfer $\mathbf{q} = \vec{k}_s - \vec{k}_i$ with finite $q_z$. This geometric effect gives rise to MTRs associated with the termination of the in-plane magnetic modulation at the surface, effectively "lifting" $\mathbf{q}$ out of the sample plane and enabling detection of lateral modulations via off-specular scattering. This is schematically illustrated in Fig. 1(b), where the in-plane propagation vectors lead to reciprocal-space features extending along $q_z$. This capability is especially relevant for detecting periodic magnetic structures with vertical modulation, such as chiral soliton lattices or other $q_z$-modulated phases that can emerge in thin films or strained heterostructures.

The attenuation length $\Lambda$ of soft x-rays is highly sensitive to the photon energy, especially across absorption edges [22]. For Mn $L_3$ edge excitation (641.3 eV), $\Lambda$ is approximately 40 nm, increasing to over 400 nm below the edge. Under grazing incidence, the effective probing depth is further reduced due to the extended in-material path length, allowing quasidepth-resolved access to the near-surface magnetic structure (illustrated in Fig. 4). In the following, we use the term "near-surface" to refer specifically to the region within the effective grazing-incidence probing depth $d_{\mathrm{eff}} \approx \Lambda \sin \alpha_i$, i.e., the topmost approximately 3–20 nm of the crystal at the Mn $L_3$ edge

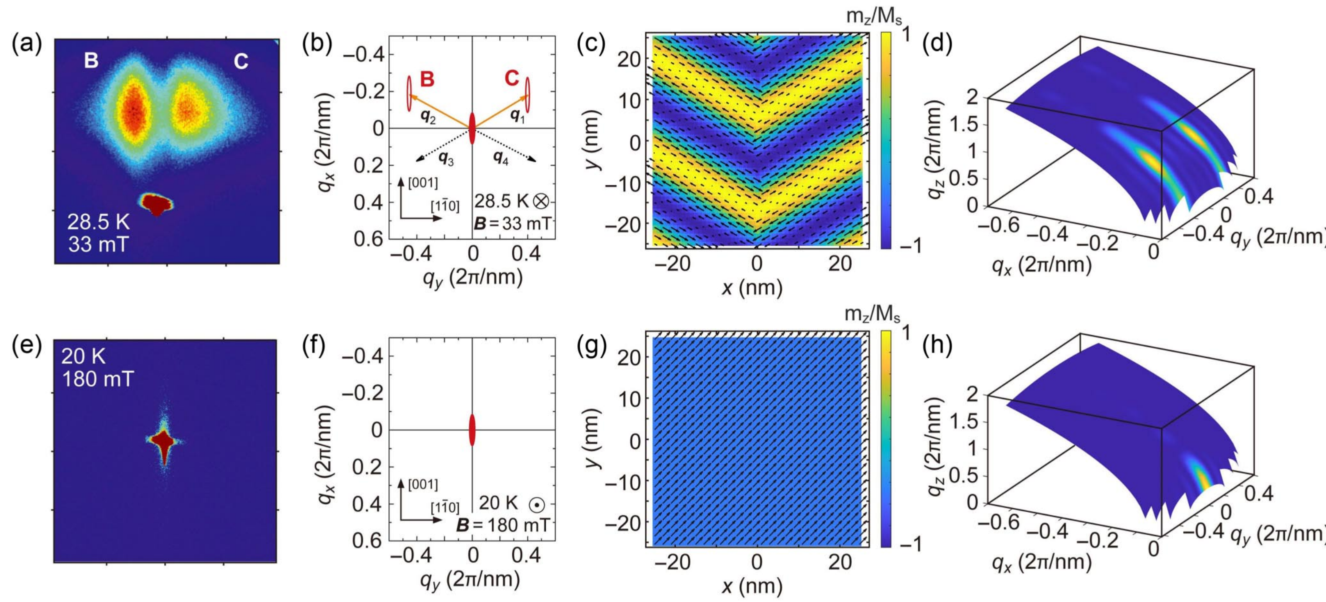


FIG. 2. Magnetic structure of the helical and conical phases revealed by GIREXS. (a–d) Helical phase at 28.5 K and 33 mT. (a) Measured GIREXS scattering pattern. The central specular reflection is accompanied by two off-specular magnetic satellite peaks (B,C), arising from helical modulations in two domains. (b) Schematic reciprocal-space representation of the accessible scattering geometry. Only those magnetic propagation vectors whose associated diffraction rods intersect the Ewald sphere on the forward-scattering side contribute to the measured intensity. (c) Simulated real-space surface magnetization texture of helical phase (two domains). (d) Corresponding simulated reciprocal-space intensity projected onto the detector plane for the experimental grazing-incidence geometry. (e–h) Conical phase at 20 K and 180 mT. (e) Experimental GIREXS scattering pattern showing only the specular reflection. (f) Schematic reciprocal-space map. (g) Simulated real-space single-domain magnetization. (h) Corresponding simulated reciprocal-space intensity, demonstrating the absence of in-plane magnetic satellites in this geometry.

for the angle range used in this work. Variation of $\alpha_i$ therefore directly modulates this probed depth. At our working angle $\alpha_i = 2.3°$, this corresponds to an effective probing depth of $d_{\text{eff}} \approx 5$ nm at the Mn $L_3$ resonance, increasing to several tens of nm when the photon energy is detuned a few eV below the edge. In the present analysis, we assume that structural and magnetic interfaces coincide and neglect additional interface roughness effects, focusing on the dominant magnetic modulation within the near-surface probing depth. For grazing-incidence geometries, surface roughness attenuates the scattered intensity through a Debye-Waller-type factor $\exp(-q_z^2\sigma^2)$. At our geometry, $q_z \approx 0.23$ nm$^{-1}$, so $\sigma \leq 1$ nm is required to retain the full signal. This tolerance is routinely achieved by mirror-polished single crystals. The clear specular peak and the Yoneda wings observed at $\alpha_f \approx 1.53°$ confirm that this condition is met by our sample. The simulated real-space magnetic structures [Figs. 2(c), 2(g), and 3(c)] are Fourier transformed to obtain the corresponding magnetic scattering intensity in reciprocal space. These reciprocal-space maps are then projected onto the calculated $q_z$ surface corresponding to a grazing-incidence angle of 1°, matching the experimental geometry. This representation captures how the magnetic diffraction rods intersect the Ewald sphere under grazing incidence and yields the projected intensity distribution on the detector [Figs. 2(d), 2(h), and 3(d)].

## III. RESULTS

To characterize the near-surface magnetic order in bulk MnSi, we employed GIREXS, optimized for detecting in-plane magnetic modulations. The [110]-oriented MnSi single crystal used in this study exhibited excellent structural quality and was previously confirmed to host a skyrmion lattice via SANS. This orientation ensures that the principal magnetic propagation vectors, especially those of the helical and skyrmion phases, lie within the surface-parallel *x*-*y* plane and are thus accessible to surface-sensitive x-ray scattering.

In the ground state [see magnetic phase diagram in Fig. 1(c)], MnSi exhibits a helical magnetic structure in which two pairs of propagation vectors are oriented along the cubic ⟨111⟩ directions [see Fig. 2(c)]. At a finite magnetic field of 180 mT, MnSi is in the conical phase at 20 K [see example shown in Fig. 2(g)]. Just below $T_C$ (at 180 mT), the system transitions into the skyrmion lattice phase, where six helices arrange into a hexagonal pattern within the plane perpendicular to the field [see Fig. 3(c)]. The field was applied out-of-plane for the measurements

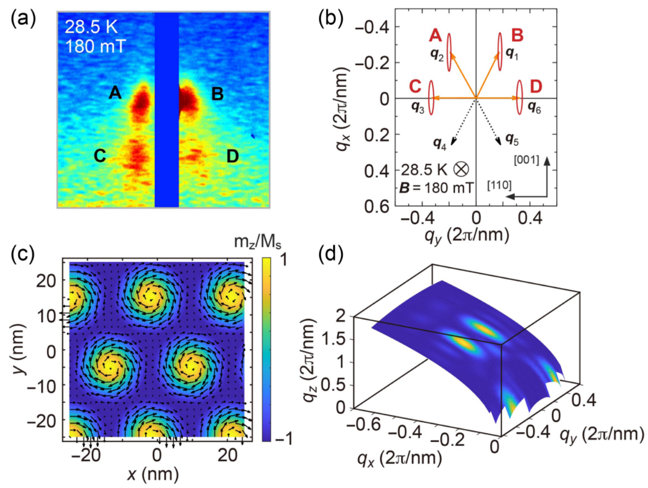


FIG. 3. Magnetic structure of the skyrmion lattice phase (at 28.5 K and 180 mT) revealed by GIREXS. (a) Experimental GIREXS scattering pattern showing four magnetic satellite peaks (A–D) associated with the ordered skyrmion lattice. (b) Schematic reciprocal-space representation of the accessible scattering geometry and the corresponding magnetic propagation vectors of the skyrmion lattice. Only the four diffraction rods intersecting the Ewald sphere on the forward-scattering side contribute to the measured intensity, whereas the remaining two are inaccessible. (c) Simulated real-space surface magnetization texture of the skyrmion lattice, illustrating the periodic arrangement of skyrmions with propagation vectors $\mathbf{q}_i$. (d) Corresponding simulated reciprocal-space intensity projected onto the detector plane for the experimental grazing-incidence geometry.

presented here, so that the helical and skyrmion propagation vectors lie within the $q_x$-$q_y$ plane.

The underlying reason GIREXS can detect these magnetic satellites arises from the nature of surface diffraction. When the incidence angle $\alpha_i$ slightly exceeds the critical angle for total external reflection (of approximately 1.5° for MnSi [57]), the x-ray beam penetrates only a few nanometers into the sample, rendering the scattering process highly surface sensitive. In this regime, the termination of the in-plane magnetic modulation at the crystal surface gives rise to MTRs extending along $q_z$. Magnetic satellites that would otherwise remain confined to the $q_x$-$q_y$ plane are therefore distributed along these rods and become experimentally accessible in off-specular geometry even in the absence of structural Bragg reflections.

Experimental validation of this surface diffraction process is provided in Fig. 2(a), which shows the GIREXS pattern measured at 28.5 K and 33 mT, where the system is in the helical phase. At an incidence angle of $\alpha_i = 2.3°$, two magnetic diffraction peaks (labeled B and C) appear symmetrically on either side of the specular spot. These features arise from two of the four helical propagation vectors $q_1$ and $q_2$, whose in-plane components satisfy the diffraction condition in this geometry. The remaining helical vectors $q_3$ and $q_4$, which project away from the surface plane, do not contribute under these conditions as their associated truncation rods do not intersect the Ewald sphere on the forward-scattering side. By mapping the scattering vectors onto the $(hk0)$ reciprocal lattice plane, we extract a modulation wavevector $q_h = (0.026 \pm 0.002)$ r.l.u. (reciprocal lattice unit $\equiv 2\pi/a$), corresponding to a real-space period of approximately 17.8 nm, in agreement with earlier SANS and LTEM studies [1,17,58]. The stated uncertainty reflects the Gaussian fit parameter. For completeness, we show the GIREXS results for the conical phase in Fig. 2(e), which resides above the helical phase when the field surpasses the first critical field. In this state, the magnetic propagation vector becomes aligned along the applied field direction, normal to the sample surface, and thus lies predominantly along $q_z$. As a result, no significant in-plane magnetic signal is observed in the surface-sensitive GIREXS geometry, as confirmed by the absence of satellite peaks; only the specular reflection remains [see Figs. 2(f)–2(h)]. In principle, this magnetic peak could be accessed at $(0, 0, q_h)$; however, the corresponding diffraction angle would be extremely small in grazing incidence, making experimental detection highly challenging.

Upon increasing the applied magnetic field to 180 mT at the same temperature just below $T_C$, the system enters the skyrmion lattice phase. The corresponding GIREXS pattern is shown in Fig. 3(a). Four magnetic diffraction peaks (A–D) emerge, arranged in reciprocal space at angular intervals of 60°, consistent with the expected hexagonal ordering of the skyrmion lattice [see reciprocal map in Fig. 3(b)]. The remaining two of the six first-order SkX peaks lie below the horizon at our chosen $\alpha_i$ and are attenuated because their truncation rods do not intersect the accessible region of reciprocal space. Note that the magnitude of the skyrmion wavevector remains unchanged from that of the helical phase, confirming that both modulations share the same periodicity. Figure 3(d) presents the result of a GIREXS contrast simulation based on the real-space skyrmion lattice structure depicted in Fig. 3(c). The simulation reproduces the expected sixfold symmetry of the visible magnetic diffraction pattern, with distinct peaks corresponding to the in-plane propagation vectors of the skyrmion lattice. The agreement with the experimental data shown in Fig. 3(a) is excellent in both angular separation and relative intensity of the diffraction peaks. The simulated pattern also includes the lower portions of peaks C and D, which are not clearly resolved in the experimental image. This discrepancy is attributed to their scattering angles falling close to or below the critical angle for total external reflection, where the x-ray beam is strongly attenuated and the effective probing depth changes rapidly.

The dependence of the scattered intensity, shown for the skyrmion phase in Fig. 4, on the incidence angle $\alpha_i$, highlights the interplay between reciprocal-space access

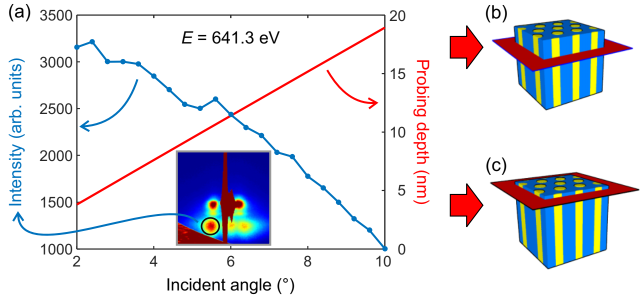


FIG. 4. Incident angle dependence of the skyrmion peak intensity, integrated over the area indicated by the blue circle in the diffraction image shown in the inset, and the corresponding probing depth at a photon energy of 641.3 eV. The schematics on the right depict the variation in probing depth for low (top) and high (bottom) incidence angles.

and surface sensitivity in GIREXS. As $\alpha_i$ increases from just above the critical angle, the measured intensity of the skyrmion peak gradually declines. This behavior reflects two competing effects: increasing $\alpha_i$ expands the region of reciprocal space intersected by the Ewald sphere, potentially allowing additional magnetic propagation vectors to contribute, while simultaneously reducing surface sensitivity due to the increased x-ray penetration depth. The probing depth, also plotted in Fig. 4, grows rapidly with increasing $\alpha_i$, consistent with this interpretation. The probing depth was computed from $\mu(E, \alpha_i)$ using tabulated MnSi optical constants [22,53] within a single-layer grazing-incidence attenuation model. At low angles, the beam probes only the near-surface region, whereas at higher angles scattering from deeper layers contributes more significantly, reducing the relative magnetic contrast associated with the surface-sensitive geometry. This angular dependence underlines the necessity of selecting $\alpha_i$ carefully to optimize signal-to-noise ratio and magnetic phase sensitivity. Despite this inherent trade-off, distinct scattering signatures of the helical, skyrmion, and conical phases can be resolved and clearly distinguished within the same experimental configuration. In the future, acquiring a series of two-dimensional slices as a function of incidence angle and temperature may enable depth-dependent reconstruction of the magnetic structure, providing experimental access to the three-dimensional character of the skyrmion lattice.

## IV. CONCLUSIONS

In this work, we have demonstrated that grazing-incidence resonant elastic x-ray scattering provides a powerful and surface-sensitive method for detecting magnetic skyrmion lattice order in bulk single crystals of MnSi. By tuning the photon energy to the Mn $L_3$ absorption edge and operating just above the critical angle, we accessed the magnetic satellites associated with the helical and skyrmion phases. This geometry enables direct observation of in-plane magnetic modulations without relying on transmission through thinned samples, thereby preserving the intrinsic bulk magnetic properties. The ability to resolve phase-specific magnetic diffraction patterns, i.e., helical, conical, and skyrmionic, under controlled variations of temperature and magnetic field demonstrates that GIREXS is well suited for studying long-range magnetic order at and near the surface. Furthermore, projection of the measured diffraction peaks into reciprocal space provides a direct link between experimental scattering patterns and real-space spin textures, offering a route toward depth-dependent reconstruction of the three-dimensional skyrmion crystal.

Our results complement and extend recent studies in specular reflection geometry, such as those performed on $Cu_2OSeO_3$ [51], where surface chiral spin textures were observed using circular dichroism contrast. Reflection-mode resonant magnetic scattering has also been successfully applied to bulk crystals, including $Cu_2OSeO_3$ [41] and $BiFeO_3$ [42], when the resonant wavelength permits access to magnetic satellites around structural Bragg reflections. In B20 compounds, such as MnSi, however, the smaller lattice parameter places the relevant structural reflections beyond the reciprocal-space range accessible at soft x-ray energies. Specular reflection therefore cannot provide access to the full skyrmion lattice under these conditions. In contrast, the grazing-incidence geometry employed here captures the magnetic diffraction signature of the skyrmion phase through magnetic truncation rods, thereby overcoming this geometrical constraint and enabling reciprocal-space mapping of the skyrmion lattice. Complementary depth profiling can be obtained with polarized neutron reflectometry (PNR), which provides Å-scale depth resolution but lacks in-plane reciprocal-space selectivity [59], whereas GIREXS resolves the in-plane magnetic satellite structure. A combined PNR-GIREXS workflow could, in future, link depth profiles to the in-plane satellite pattern without thinning bulk crystals.

GIREXS is complementary to existing 3D-nanomagnetism techniques [60]. Real-space methods, such as hard-x-ray magnetic vector tomography [61], soft-x-ray magnetic laminography [62], and Lorentz-TEM tomography, deliver full 3D reconstructions but require pillar, thinned, or electron-transparent specimens, with spatial resolutions in the range of approximately 50–100 nm. In reciprocal space, field-dependent and depth-resolved XRMS in multilayers has recently been demonstrated [63], establishing reciprocal-space depth profiling at the nm scale. GIREXS uniquely combines reciprocal-space resolution of the magnetic satellite pattern, element-specific resonant contrast, and nm-scale depth tunability while operating on unthinned bulk crystals, whose magnetic phase diagram remains unmodified by dimensional confinement.

In summary, GIREXS provides a versatile, element-specific, and nondestructive approach for studying complex spin structures in bulk crystals, including chiral magnets where fixed-energy soft-x-ray REXS does not provide access to magnetic satellite reflections. Its compatibility with various sample environments and its ability to distinguish between competing magnetic phases make it a promising technique for future investigations of chiral magnetism, surface-induced phenomena, and the dimensional crossover from 2D to 3D skyrmion states across a wide class of materials.

## ACKNOWLEDGMENTS

We thank Diamond Light Source for beamtime on beamline I10 under proposals SI8703, SI9117, and SI9595. S. L. Z. and T. H. acknowledge financial support by Engineering and Physical Sciences Research Council (EPSRC) (EP/N032128/1). This study received funding from the Deutsche Forschungsgemeinschaft (DFG, German Research Foundation) under TRR80 (From Electronic Correlations to Functionality, Project No. 107745057), TRR360 (Constrained Quantum Matter, Project No. 492547816, Projects C1 and C3), SPP2137 (Skyrmionics, Project No. 403191981, Grant No. PF393/19), and the excellence cluster MCQST under Germany's Excellence Strategy EXC-2111 (Project No. 390814868). Financial support by the European Research Council (ERC) through Advanced Grants No. 291079 (TOPFIT) and No. 788031 (ExQuiSid) is gratefully acknowledged.

## DATA AVAILABILITY

The data that support the findings of this article are shown in the figures. The raw experimental data supporting this study have been deposited in Zenodo and are available at Ref. 64.


[1] S. Mühlbauer, B. Binz, F. Jonietz, C. Pfleiderer, A. Rosch, A. Neubauer, R. Georgii, and P. Böni, Skyrmion lattice in a chiral magnet, Science **323**, 915 (2009).

[2] A. Neubauer, C. Pfleiderer, B. Binz, A. Rosch, R. Ritz, P. G. Niklowitz, and P. Böni, Topological Hall effect in the *A* phase of MnSi, Phys. Rev. Lett. **102**, 186602 (2009).

[3] N. Nagaosa and Y. Tokura, Emergent electromagnetism in solids, Phys. Scr. T **146**, 014020 (2012).

[4] N. Nagaosa and Y. Tokura, Topological properties and dynamics of magnetic skyrmions, Nat. Nanotech. **8**, 899 (2013).

[5] W. Münzer, A. Neubauer, T. Adams, S. Mühlbauer, C. Franz, F. Jonietz, R. Georgii, P. Böni, B. Pedersen, M. Schmidt, A. Rosch, and C. Pfleiderer, Skyrmion lattice in the doped semiconductor $Fe_{1-x}Co_xSi$, Phys. Rev. B **81**, 041203(R) (2010).

[6] X. Z. Yu, Y. Onose, N. Kanazawa, J. H. Park, J. H. Han, Y. Matsui, N. Nagaosa, and Y. Tokura, Real-space observation of a two-dimensional skyrmion crystal, Nature (London) **465**, 901 (2010).

[7] T. Yokouchi, N. Kanazawa, A. Tsukazaki, Y. Kozuka, M. Kawasaki, M. Ichikawa, F. Kagawa, and Y. Tokura, Stability of two-dimensional skyrmions in thin films of $Mn_{1-x}Fe_xSi$ investigated by the topological hall effect, Phys. Rev. B **89**, 064416 (2014).

[8] H. Wilhelm, M. Baenitz, M. Schmidt, U. K. Rößler, A. A. Leonov, and A. N. Bogdanov, Precursor phenomena at the magnetic ordering of the cubic helimagnet FeGe, Phys. Rev. Lett. **107**, 127203 (2011).

[9] X. Z. Yu, N. Kanazawa, Y. Onose, K. Kimoto, W. Z. Zhang, S. Ishiwata, Y. Matsui, and Y. Tokura, Near room-temperature formation of a skyrmion crystal in thin-films of the helimagnet FeGe, Nat. Mater. **10**, 106 (2011).

[10] K. Shibata, X. Z. Yu, T. Hara, D. Morikawa, N. Kanazawa, K. Kimoto, S. Ishiwata, Y. Matsui, and Y. Tokura, Towards control of the size and helicity of skyrmions in helimagnetic alloys by spin–orbit coupling, Nat. Nanotech. **8**, 723 (2013).

[11] N. Kanazawa, J.-H. Kim, D. S. Inosov, J. S. White, N. Egetenmeyer, J. L. Gavilano, S. Ishiwata, Y. Onose, T. Arima, B. Keimer, and Y. Tokura, Possible skyrmion-lattice ground state in the B20 chiral-lattice magnet MnGe as seen via small-angle neutron scattering, Phys. Rev. B **86**, 134425 (2012).

[12] S. Seki, X. Z. Yu, S. Ishiwata, and Y. Tokura, Observation of skyrmions in a multiferroic material, Science **336**, 198 (2012).

[13] Y. Guang, Y. Fujishiro, A. Tanaka, L. Peng, Y. Kaneko, N. Kanazawa, Y. Tokura, and X. Yu, Topological stability of spin textures in Si/Co-doped helimagnet FeGe, J. Phys. Mater. **7**, 025009 (2024).

[14] F. Jonietz, S. Mühlbauer, C. Pfleiderer, A. Neubauer, W. Münzer, A. Bauer, T. Adams, R. Georgii, P. Böni, R. A. Duine, K. Everschor, M. Garst, and A. Rosch, Spin transfer torques in MnSi at ultralow current densities, Science **330**, 1648 (2010).

[15] C. Pappas, E. Lelièvre-Berna, P. Falus, P. M. Bentley, E. Moskvin, S. Grigoriev, P. Fouquet, and B. Farago, Chiral paramagnetic skyrmion-like phase in MnSi, Phys. Rev. Lett. **102**, 197202 (2009).

[16] C. Pappas, L. J. Bannenberg, E. Lelièvre-Berna, F. Qian, C. D. Dewhurst, R. M. Dalgliesh, D. L. Schlagel, T. A. Lograsso, and P. Falus, Magnetic fluctuations, precursor phenomena, and phase transition in MnSi under a magnetic field, Phys. Rev. Lett. **119**, 047203 (2017).

[17] A. Tonomura, X. Yu, K. Yanagisawa, T. Matsuda, Y. Onose, N. Kanazawa, H. S. Park, and Y. Tokura, Real-space observation of skyrmion lattice in helimagnet MnSi thin samples, Nano Lett. **12**, 1673 (2012).

[18] H. Du, R. Che, L. Kong, X. Zhao, C. Jin, C. Wang, J. Yang, W. Ning, R. Li, C. Jin, X. Chen, J. Zang, Y. Zhang, and M. Tian, Edge-mediated skyrmion chain and its collective dynamics in a confined geometry, Nat. Commun. **6**, 8504 (2015).

[19] F. Zheng, F. N. Rybakov, A. B. Borisov, D. Song, S. Wang, Z.-A. Li, H. Du, N. S. Kiselev, J. Caron, A. Kovács, M. Tian, Y. Zhang, S. Blügel, and R. E. Dunin-Borkowski, Experimental observation of chiral magnetic bobbers in B20-type FeGe, Nat. Nanotechnol. **13**, 451 (2018).

[20] P. Milde, D. Köhler, J. Seidel, L. M. Eng, A. Bauer, A. Chacon, J. Kindervater, S. Mühlbauer, C. Pfleiderer, S. Buhrandt, C. Schütte, and A. Rosch, Unwinding of a skyrmion lattice by magnetic monopoles, Science **340**, 1076 (2013).
[21] J. P. Hannon, G. T. Trammell, M. Blume, and D. Gibbs, X-ray resonance exchange scattering, Phys. Rev. Lett. **61**, 1245 (1988).
[22] G. van der Laan, Soft X-ray resonant magnetic scattering of magnetic nanostructures, C. R. Phys. **9**, 570 (2008).
[23] D. M. Burn, S. Zhang, K. Zhai, Y. Chai, Y. Sun, G. van der Laan, and T. Hesjedal, Mode-resolved detection of magnetization dynamics using x-ray diffractive ferromagnetic resonance, Nano Lett. **20**, 345 (2019).
[24] M. Blume and D. Gibbs, Polarization dependence of magnetic x-ray scattering, Phys. Rev. B **37**, 1779 (1988).
[25] D. Gibbs, D. R. Harshman, E. D. Isaacs, D. B. McWhan, D. Mills, and C. Vettier, Polarization and resonant properties of magnetic x-ray scattering in holmium, Phys. Rev. Lett. **61**, 1241 (1988).
[26] S. L. Zhang, G. van der Laan, and T. Hesjedal, Direct experimental determination of spiral spin structures via the dichroism extinction effect in resonant elastic soft x-ray scattering, Phys. Rev. B **96**, 094401 (2017).
[27] S. L. Zhang, G. van der Laan, and T. Hesjedal, Direct experimental determination of the topological winding number of skyrmions in $Cu_2OSeO_3$, Nat. Commun. **8**, 14619 (2017).
[28] S. Zhang, G. van der Laan, W. Wang, A. Haghighirad, and T. Hesjedal, Direct observation of twisted surface skyrmions in bulk crystals, Phys. Rev. Lett. **120**, 227202 (2018).
[29] J.-Y. Chauleau, W. Legrand, N. Reyren, D. Maccariello, S. Collin, H. Popescu, K. Bouzehouane, V. Cros, N. Jaouen, and A. Fert, Chirality in magnetic multilayers probed by the symmetry and the amplitude of dichroism in X-ray resonant magnetic scattering, Phys. Rev. Lett. **120**, 037202 (2018).
[30] W. Legrand, J.-Y. Chauleau, D. Maccariello, N. Reyren, S. Collin, K. Bouzehouane, N. Jaouen, V. Cros, and A. Fert, Hybrid chiral domain walls and skyrmions in magnetic multilayers, Sci. Adv. **4**, eaat0415 (2018).
[31] C. Léveillé, S. Flewett, E. Burgos-Parra, Y. Sassi, W. Legrand, F. Ajejas, V. Cros, N. Reyren, and N. Jaouen, Chiral spin spiral in synthetic antiferromagnets probed by circular dichroism in x-ray resonant magnetic scattering, Phys. Rev. B **104**, L060402 (2021).
[32] C. Léveillé, E. Burgos-Parra, Y. Sassi, F. Ajejas, V. Chardonnet, E. Pedersoli, F. Capotondi, G. De Ninno, F. Maccherozzi, S. Dhesi, D. M. Burn, G. van der Laan, O. S. Latcham, A. V. Shytov, V. V. Kruglyak, E. Jal, V. Cros, J.-Y. Chauleau, N. Reyren, M. Viret, and N. Jaouen, Ultrafast time-evolution of chiral Néel magnetic domain walls probed by circular dichroism in x-ray resonant magnetic scattering, Nat. Commun. **13**, 1412 (2022).
[33] A. Fasolino, P. Carra, and M. Altarelli, X-ray resonant magnetic scattering from surfaces, Phys. Rev. B **47**, 3877 (1993).
[34] G. M. Watson, D. Gibbs, J. P. Hill, and J. C. Lang, X-ray scattering study of the magnetic structure near the (001) surface of $UO_2$, Phys. Rev. Lett. **77**, 751 (1996).
[35] S. Langridge, G. M. Watson, D. Gibbs, J. J. Betouras, N. I. Gidopoulos, F. Pollmann, M. W. Long, C. Vettier, and G. H. Lander, Distinct magnetic phase transition at the surface of an antiferromagnet, Phys. Rev. Lett. **112**, 167201 (2014).
[36] R. M. Osgood, S. K. Sinha, J. W. Freeland, Y. U. Idzerda, and S. D. Bader, X-ray scattering from magnetically and structurally rough surfaces, J. Magn. Magn. Mater. **198-199**, 698 (1999).
[37] D. R. Lee, S. K. Sinha, D. Haskel, Y. Choi, J. C. Lang, S. A. Stepanov, and G. Srajer, X-ray resonant magnetic scattering from structurally and magnetically rough interfaces in multilayered systems. I. Specular reflectivity, Phys. Rev. B **68**, 224409 (2003).
[38] A. Amato, P. Dalmas de Réotier, D. Andreica, A. Yaouanc, A. Suter, G. Lapertot, I. M. Pop, E. Morenzoni, P. Bonfà, F. Bernardini, and R. De Renzi, Understanding the $\mu$ SR spectra of MnSi without magnetic polarons, Phys. Rev. B **89**, 184425 (2014).
[39] B. Lebech, J. Bernhard, and T. Freltoft, Magnetic structures of cubic FeGe studied by small-angle neutron scattering, J. Phys.: Condens. Matter **1**, 6105 (1989).
[40] H. Effenberger and F. Pertlik, Die Kristallstrukturen der Kupfer(II)-oxo-selenite $Cu_2O(SeO_3)$ (kubisch und monoklin) und $Cu_4O(SeO_3)_3$ (monoklin und triklin); [The crystal structures of the copper(II)-oxo-selenites $Cu_2O(SeO_3)$ (cubic and monoclinic), and $Cu_4O(SeO_3)_3$ (monoclinic and triclinic)], Monatsh. Chem. **117**, 887 (1986).
[41] S. L. Zhang, A. Bauer, H. Berger, C. Pfleiderer, G. van der Laan, and T. Hesjedal, Resonant elastic x-ray scattering from the skyrmion lattice in $Cu_2OSeO_3$, Phys. Rev. B **93**, 214420 (2016).
[42] A. Finco, A. Haykal, S. Fusil, P. Kumar, P. Dufour, A. Forget, D. Colson, J.-Y. Chauleau, M. Viret, N. Jaouen, V. Garcia, and V. Jacques, Imaging topological defects in a noncollinear antiferromagnet, Phys. Rev. Lett. **128**, 187201 (2022).
[43] Y. Yamasaki, D. Morikawa, T. Honda, H. Nakao, Y. Murakami, N. Kanazawa, M. Kawasaki, T. Arima, and Y. Tokura, Dynamical process of skyrmion-helical magnetic transformation of the chiral-lattice magnet FeGe probed by small-angle resonant soft x-ray scattering, Phys. Rev. B **92**, 220421 (2015).
[44] D. M. Burn, S. Wang, W. Wang, G. van der Laan, S. Zhang, H. Du, and T. Hesjedal, Field and temperature dependence of the Skyrmion lattice phase in chiral magnet membranes, Phys. Rev. B **101**, 014446 (2020).
[45] Y. Okamura, Y. Yamasaki, D. Morikawa, T. Honda, V. Ukleev, H. Nakao, Y. Murakami, K. Shibata, F. Kagawa, S. Seki, T. Arima, and Y. Tokura, Directional electric-field induced transformation from skyrmion lattice to distinct helices in multiferroic $Cu_2OSeO_3$, Phys. Rev. B **95**, 184411 (2017).
[46] V. Ukleev, Y. Yamasaki, D. Morikawa, K. Karube, K. Shibata, Y. Tokunaga, Y. Okamura, K. Amemiya, M. Valvidares, H. Nakao, Y. Taguchi, Y. Tokura, and T. Arima, Element-specific soft x-ray spectroscopy, scattering, and imaging studies of the skyrmion-hosting compound $Co_8Zn_8Mn_4$, Phys. Rev. B **99**, 144408 (2019).
[47] V. Ukleev, O. I. Utesov, C. Luo, F. Radu, S. Wintz, M. Weigand, S. Finizio, M. Winter, A. Tahn, B. Rellinghaus,

K. Karube, Y. Tokura, Y. Taguchi, and J. S. White, Competing anisotropies in the chiral cubic magnet $Co_8Zn_8Mn_4$ unveiled by resonant x-ray magnetic scattering, Phys. Rev. B **109**, 184415 (2024).
[48] Y. Okamura, Y. Yamasaki, D. Morikawa, T. Honda, V. Ukleev, H. Nakao, Y. Murakami, K. Shibata, F. Kagawa, S. Seki, T. Arima, and Y. Tokura, Emergence and magnetic-field variation of chiral-soliton lattice and skyrmion lattice in the strained helimagnet $Cu_2OSeO_3$, Phys. Rev. B **96**, 174417 (2017).
[49] M. T. Birch *et al.*, Real-space imaging of confined magnetic skyrmion tubes, Nat. Commun. **11**, 1726 (2020).
[50] S. L. Zhang, I. Stasinopoulos, T. Lancaster, F. Xiao, A. Bauer, F. Rucker, A. A. Baker, A. I. Figueroa, Z. Salman, F. L. Pratt, S. J. Blundell, T. Prokscha, A. Suter, J. Waizner, M. Garst, D. Grundler, G. van der Laan, C. Pfleiderer, and T. Hesjedal, Room-temperature helimagnetism in FeGe thin films, Sci. Rep. **7**, 123 (2017).
[51] V. Ukleev, C. Luo, R. Abrudan, A. Aqeel, C. H. Back, and F. Radu, Chiral surface spin textures in $Cu_2OSeO_3$ unveiled by soft X-ray scattering in specular reflection geometry, Sci. Technol. Adv. Mater. **23**, 682 (2022).
[52] K. Ran, W. Tan, X. Sun, Y. Liu, R. M. Dalgliesh, N.-J. Steinke, G. van der Laan, S. Langridge, T. Hesjedal, and S. Zhang, Bending skyrmion strings under two-dimensional thermal gradients, Nat. Commun. **15**, 4860 (2024).
[53] J. Fink, E. Schierle, E. Weschke, and J. Geck, Resonant elastic soft x-ray scattering, Rep. Prog. Phys. **76**, 056502 (2013).
[54] G. Renaud, R. Lazzari, and F. Leroy, Probing surface and interface morphology with grazing incidence small angle x-ray scattering, Surf. Sci. Rep. **64**, 255 (2009).
[55] A. Hexemer and P. Müller-Buschbaum, Advanced grazing-incidence techniques for modern soft-matter materials analysis, IUCrJ **2**, 106 (2015).
[56] S. Stanescu, C. Mocuta, F. Merlet, and A. Barbier, Two-dimensional resonant magnetic soft X-ray scattering set-up for extreme sample environment, J. Synchrotron Rad. **20**, 181 (2013).
[57] B. L. Henke, E. M. Gullikson, and J. C. Davis, X-ray interactions: Photoabsorption, scattering, transmission, and reflection at $E = 50 - 30000$ eV, $Z = 1 - 92$, At. Data Nucl. Data Tables **54**, 181 (1993).
[58] T. Adams, S. Mühlbauer, C. Pfleiderer, F. Jonietz, A. Bauer, A. Neubauer, R. Georgii, P. Böni, U. Keiderling, K. Everschor, M. Garst, and A. Rosch, Long-range crystalline nature of the skyrmion lattice in MnSi, Phys. Rev. Lett. **107**, 217206 (2011).
[59] G. L. Causer, Opportunities for near-surface small-angle neutron scattering to probe magnetic nanostructures within thin-film volumes, J. Appl. Crystallogr. **58**, 1455 (2025).
[60] A. Fernández-Pacheco, R. Streubel, O. Fruchart, R. Hertel, P. Fischer, and R. P. Cowburn, Three-dimensional nanomagnetism, Nat. Commun. **8**, 15756 (2017).
[61] C. Donnelly, M. Guizar-Sicairos, V. Scagnoli, S. Gliga, M. Holler, Jörg Raabe, and L. J. Heyderman, Three-dimensional magnetization structures revealed with X-ray vector nanotomography, Nature (London) **547**, 328 (2017).
[62] K. Witte, A. Späth, S. Finizio, C. Donnelly, B. Watts, B. Sarafimov, M. Odstrcil, M. Guizar-Sicairos, M. Holler, R. H. Fink, and Jörg Raabe, From 2D STXM to 3D imaging: Soft X-ray laminography of thin specimens, Nano Lett. **20**, 1305 (2020).
[63] E. Burgos-Parra, Y. Sassi, W. Legrand, F. Ajejas, C. Léveillé, P. Gargiani, M. Valvidares, N. Reyren, V. Cros, N. Jaouen, and S. Flewett, Probing of three-dimensional spin textures in multilayers by field dependent X-ray resonant magnetic scattering, Sci. Rep. **13**, 11711 (2023).
[64] J. Chen, A. Bauer, C. Pfleiderer, G. van der Laan, T. Hesjedal, and S. Zhang, Raw experimental data for: Grazing-incidence resonant elastic x-ray scattering of skyrmion lattices in bulk MnSi, Zenodo https://doi.org/10.5281/zenodo.21335609 (2026).